

An Aluminum-Benzo[1,2-b:4,5-b']dithiophene-4,8-dione Organic Rechargeable Battery Featuring Low Self-Discharge

Yijia Wang,^[a] Kok Long Ng,^[b] and Gisele Azimi^{*[a, b]}

The achievable cell-level specific energy density of existing aluminum-ion batteries (AIBs) employing AlCl_4^- intercalation type cathodes is intrinsically limited by the chloroaluminate anolyte. Towards achieving AIBs with higher specific energy, it is imperative to explore alternative cell chemistries that fundamentally tap the capacity of Al metal anode. Here, we report a benzo[1,2-b:4,5-b']dithiophene-4,8-dione (BDTD) organic electrode material with favorable AlCl_2^+ intercalation mecha-

nism. This BDTD cathode delivers a specific capacity of 143 mAh g^{-1} , and the resulting battery exhibits a well-defined voltage plateau at $\sim 1.2 \text{ V}$. This characteristic voltage plateau is mainly driven by the predominant diffusive charge storage in BDTD cathode, which accounts for up to 85% of the total charge-storage contribution. As a result, the BDTD cathode demonstrates exceptional self-discharging resistance by recovering $> 95\%$ of its capacity upon 24-h resting.

The widespread adoption of electric vehicles (EVs) and the rapid development of renewable energy technologies are pivotal strategies to address the decarbonization challenges.^[1,2] Lithium-ion batteries (LIBs) have been vastly adopted in these applications owing to their high specific energy ($> 250 \text{ Wh kg}^{-1}$) and high efficiency in storing as well as dispatching electrical energy for on-demand utilization.^[3] Largely driven by the ever-growing demands for LIBs, the concomitant supply risks associated with the critical raw materials utilized in LIB chemistry, such as lithium and cobalt, have raised concerns on the long-term sustainability of existing LIB technologies.^[3–5] Consequently, alternative battery chemistries that are sustainable, inexpensive, and safe, are highly desired.^[6]

The high natural abundance, low cost, high gravimetric and volumetric capacity (2981 mAh g^{-1} and 8046 mAh cm^{-3} , respectively) of aluminum (Al) metal, render Al-based batteries an attractive candidate amongst various post-lithium energy storage systems.^[7–9] In 2015, Dai et al. developed an aluminum-ion battery (AIB) using AlCl_4^- intercalation type 3D graphitic foam as the cathode and chloroaluminate ionic liquid (IL) as the electrolyte/anolyte. The battery delivered a stable capacity of 60 mAh g^{-1} for over 7500 cycles at 4000 mA g^{-1} .^[10] Inspired by this cornerstone study, the past several years have witnessed a remarkable surge of research publications on AIBs.^[8,9] For AIBs employing AlCl_4^- intercalation type cathodes, it is crucial to acknowledge that the chloroaluminate IL simultaneously serves as (i) a medium for ion transportation, and, (ii) a source of electroactive Al_2Cl_7^- and AlCl_4^- species,

which is the key component that enables reversible Al deposition/stripping. This unique functionalities of chloroaluminate ILs inevitably compromises the achievable cell-level capacity and specific energy density of resulting batteries, largely due to intrinsically low capacity of chloroaluminate ILs. For instance, the theoretical capacity of the commonly used IL prepared by mixing aluminum chloride (AlCl_3) and 1-ethyl-3-methylimidazolium chloride (EMImCl) at molar ratio of 1.3, is limited to 19 mAh g^{-1} in AIBs employing AlCl_4^- intercalation type cathodes.^[11,12]

To truly benefit from the high gravimetric- and volumetric capacity of employing Al metal anode, research attention has gradually shifted toward exploring cathode materials that interact with Al-containing cations (e.g., Al^{3+} , AlCl_2^+ and AlCl_2^{2+}) to achieve charge storage, as the capacity of Al metal anode can be partially-, or even fully accessed, in these systems. Notably, many battery systems employing Al^{3+} intercalation- and conversion type cathode materials are known to fully access the capacity of Al metal anode.^[9] However, factors such as slow $\text{Al}_2\text{Cl}_7^- \rightarrow \text{Al}^{3+}$ dissociation kinetics, sluggish solid-state Al^{3+} migration kinetics, and strong electrostatic interactions between Al^{3+} and ionic host lattice,^[13,14] adversely affect the rate performance, stability, and operating voltage of these battery systems.^[15–17] Besides energy density, the self-discharge behavior represents another critical aspect that is often neglected, but of extreme importance toward practical application of AIBs,^[9] given most commercial EVs remain idle for 90% of the time.^[18] To date, very few studies investigated the self-discharge behavior of AIBs.^[19–25] For the widely adopted graphitic/carbonaceous cathodes, the self-discharge rates can be as high as $16.82\% \text{ h}^{-1}$.^[25] For these reasons, the investigation of alternative electrode chemistries that demonstrate balanced performance in terms of cell-level specific energy density, rate performance, and self-discharge rates, are highly desired.

In this study, benzo[1,2-b:4,5-b']dithiophene-4,8-dione (BDTD) is investigated as a potential organic cathode material for AIBs. Organic electrode materials consist of earth-abundant light elements such as C, H, O, and S offer opportunities for

[a] Y. Wang, Prof. G. Azimi
Department of Chemical Engineering and Applied Chemistry
University of Toronto
200 College Street, M5S 3E5 Toronto, Ontario, Canada
E-mail: g.azimi@utoronto.ca

[b] K. Long Ng, Prof. G. Azimi
Department of Materials Science and Engineering
University of Toronto
184 College Street, M5S 3E4 Toronto, Ontario, Canada

 Supporting information for this article is available on the WWW under <https://doi.org/10.1002/batt.202200182>

developing sustainable and energy-dense storage devices.^[26] Many reported organic electrode materials are subjected to dissolution in chloroaluminate ILs.^[27] To alleviate unintended shuttling of the soluble BDTD species (Supporting Information Figure S1), and simultaneously improve overall conductivity of the cell, a modified membrane strategy using Super PTM conductive carbon is proposed. The chloroaluminate IL prepared by mixing AlCl₃ and trimethylamine hydrochloride (TMAHCl) at a molar ratio of 1.8 was used as the electrolyte. Compared with the widely adopted EMImCl-based chloroaluminate IL electrolyte, the higher anolyte capacity of the AlCl₃-TMAHCl electrolyte due to the lower molar mass of TMAHCl (Supporting Information Figure S2) and the lower cost of TMAHCl further enhance the performance and sustainability of the resulting battery systems.^[28] A schematic of the assembled cell and mechanism is presented in Figure 1(a). During cycling, the reversible intercalation/deintercalation of AlCl₂⁺ was achieved at the carbonyl sites (C=O) of BDTD, contribute to the reversible capacity over cycles (Figure 1a).

The pristine BDTD crystals exhibit irregular elongated plate-like morphology with sizes ranging from several microns to around 100 μm (Figure 1b). The Fourier-transform infrared spectroscopy (FT-IR) absorption bands at around 3092 and 3075 cm⁻¹, can be attributed to the C-H vibrations of the heteroaromatic rings (Figure 1c). The absorption peaks

located at around 1646, 1281, and 1192 cm⁻¹ correspond to the C=O vibrations.^[29,30] The absorption bands at around 835 and 724 cm⁻¹ can be assigned to the stretching vibration and in-plane deformation vibration of the C-S of the thiophene ring.^[29] The as-prepared Super PTM-modified membrane has a deposited carbon layer of less than 30 μm thick (Figure 1d). The experimentally determined X-ray diffraction (XRD) pattern closely matches that of the simulated pattern (Supporting Information Figure S3).^[31] The distinct and strong peaks indicate the polycrystallinity of the BDTD. Minor deviations observed from the relative peak intensity may be due to the presence of impurities.

Before evaluating the electrochemical performance of the cell employing the Super PTM-modified membrane, the electrochemical activity of the modified membrane was first examined. The modified membrane demonstrated limited current response relative to that of BDTD, thus confirming its negligible current/capacity contribution to overall battery performance (Figure 2a). We further investigated the cells utilizing unmodified- and Super PTM-modified membrane using electrochemical impedance spectroscopy (EIS). As shown in Figure 2(b), both systems consist of one depressed semi-circle in the medium-to-high frequency region and a sloped line in the low frequency region. An equivalent circuit (Figure 2b, inset) is constructed to account for the characteristics of the systems, in which R_e

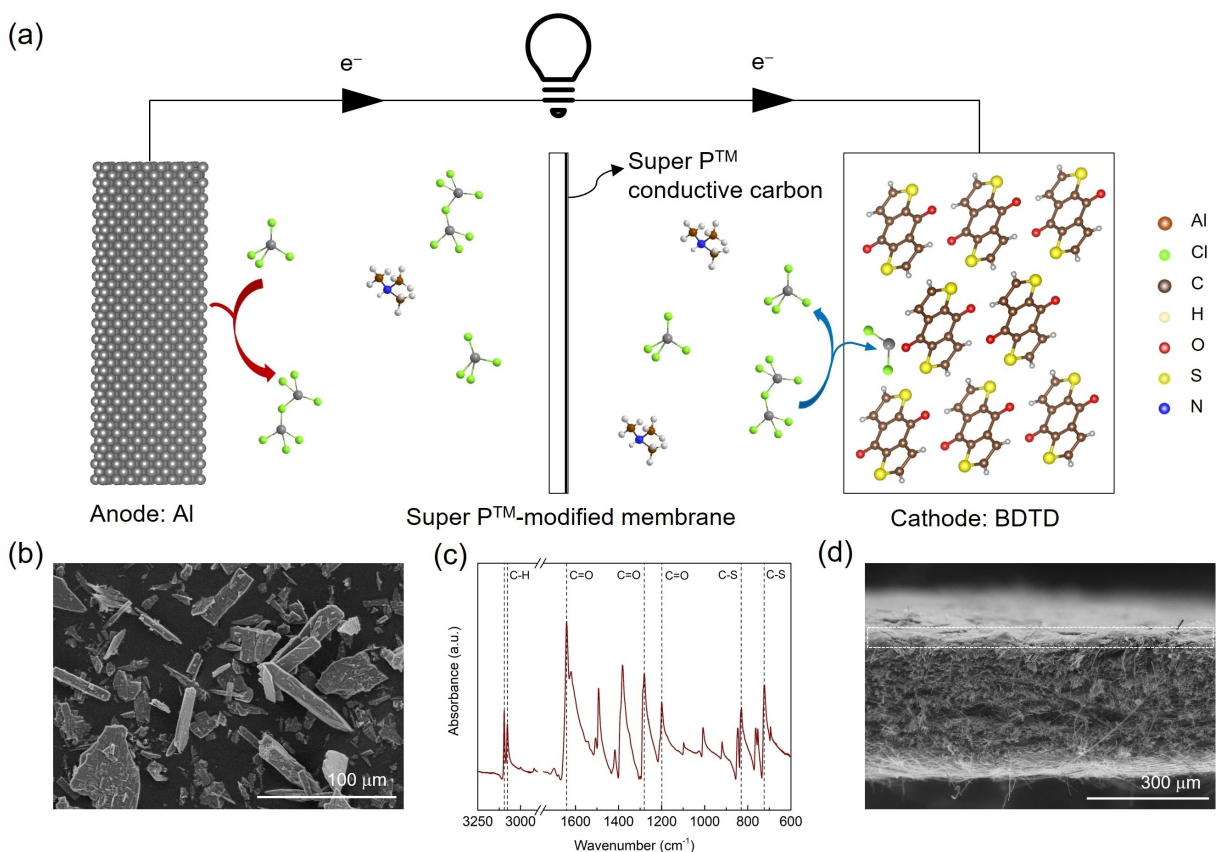


Figure 1. a) Schematic illustration of the Al | BDTD battery employing Super PTM-modified membrane. b) The secondary electron (SE) image of the pristine BDTD. c) The FT-IR spectrum of the pristine BDTD. d) The cross-sectional SE image of the Super PTM-modified membrane. Dashed region: super PTM carbon layer.

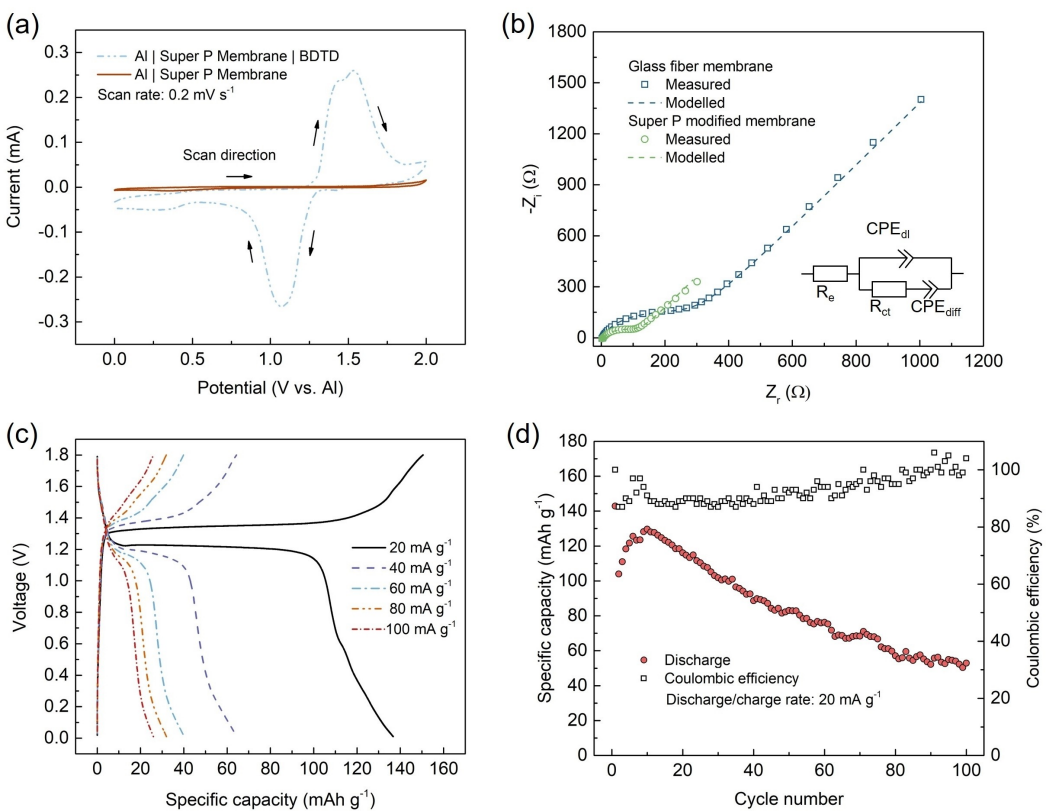


Figure 2. a) Electrochemical activity of the modified membrane measured at 0.2 mV s^{-1} . b) The Nyquist plot of the batteries utilizing glass fiber membrane and the modified membrane. c) Voltage profiles at discharging/charging rates of 20, 40, 60, 80, and 100 mA g^{-1} . d) Galvanostatic long term cycling performance at 20 mA g^{-1} .

represents the solution resistance, and CPE_{dl} and R_{ct} correspond to the capacitance and the interface charge transfer resistance of the BDTD electrode. A constant phase element (CPE_{diff}) is used to model the diffusion of the electroactive species into the BDTD electrode.^[32] The corresponding Bode plots for the two systems are presented (Supporting Information Figure S4), in which only one inflection point was found for both systems, indicating that only one time constant is present. The fitted values for each circuit element are tabulated in Supporting Information Table S1. A much lower R_{ct} value was observed for the battery that utilizes Super PTM-modified membrane (120.8Ω) compared with the unmodified counterpart (299.9Ω). It is inferred that the highly conductive Super PTM carbon layer facilitates the interface charge transfer process.

To evaluate the electrochemical performance of the BDTD electrode in chloroaluminate IL electrolyte, rate performance and long-term cycling tests were conducted. The voltage profiles of the BDTD discharging/charging at 20, 40, 60, 80 and 100 mA g^{-1} , are presented in Figure 2(c). The BDTD electrode can deliver discharge capacities of 137, 65, 40, 32 and 26 mAh g^{-1} at current densities of 20, 40, 60, 80 and 100 mA g^{-1} , respectively. It is notable to mention that the BDTD electrode demonstrates a low discharging and charging voltage polarization of less than 0.23 V at 20 mA g^{-1} (measured at 100 mA g^{-1}), which is significantly lower than many inorganic cathode materials reported in ALBs.^[20,33–35] The complete rate

capability test is presented in Supporting Information Figure S5.

The long-term cycling test was conducted at 20 mA g^{-1} and the results are shown in Figure 2(d). The BDTD electrode delivered an initial capacity of 143 mAh g^{-1} (Supporting Information Figure S6). After 100 cycles, 50 mAh g^{-1} was retained. The Coulombic efficiency gradually increased from an initial value of 87% to 100% over cycles. In this study, a Super PTM-modified membrane was introduced as an adsorption layer sandwiching the active material with the molybdenum current collector to inhibit the shuttling of the dissolved active material. The long-term cycling performance of a cell employing the normal glass fiber membrane was included as a comparison in Supporting Information Figure S7, in which the cell employing the Super PTM-modified membrane demonstrates substantial improvement in its cycling performance. Similar phenomenon had been reported in non-aqueous Na-ion battery system before, in which the cycling performance of the organic sodium salt of tetracyanoquinodimethane had been greatly improved due to the barrier effect of the carbon adsorption layer on the membrane separator.^[36] This highly conductive carbon layer also serves as an upper current collector and increases the utilization of the active material.^[36] In Supporting Information Figure S7, the cell adopting the normal glass fiber membrane only delivered a capacity of 59 mAh g^{-1} in the first discharge, which can be reasonably

ascribed to i) the shuttling of active material due to the absence of the Super PTM-modified membrane and ii) the lack of conductive carbon interface to enhance the active material utilization. Compared with the cell utilizing the Super PTM-modified membrane, the capacity of the cell using the normal membrane declines rapidly to below 50 mAh g⁻¹ after 17 cycles, showing that the adoption of Super PTM-modified membrane greatly enhances the electrochemical performance and stability of batteries employing the BDTD electrode.

To examine the intercalating species, the pristine, discharged and the charged electrodes were characterized using X-ray photoelectron spectroscopy (XPS). The full survey spectra of the pristine- and the discharged electrodes are presented in Figure 3a. The emergence of the strong Al 2p and Cl 2p signals in the spectrum of the discharged electrodes suggest the intercalation of the aluminum complex ions. As the N 1s signal

on the discharged spectrum is undistinguishable from the background, this indicates the interacting ion is unlikely to be protonated trimethylamine ion (TMAH^+). As shown in Supporting Information Figure S8, no shift in S 2p signal is observed in the discharged BDTD electrode relative to that of the pristine BDTD electrode, suggesting that S is not involved in the redox process. The weakened S 2p signal from the discharged electrode is mainly attributed to the loss of active material over cycles. The higher Al 2p and Cl 2p signals at the discharged state compared with that in the charged state can be ascribed to the reversible insertion of the chloroaluminate complex (Figure 3b and c). The peak at around 75 eV in the Al 2p branches and the peak at around 199 eV in the Cl 2p branches can be assigned to the intercalated AlCl_2^{+} ^[37]. The reversible charge storage on organic electrode materials with carbonyl group (C=O) is usually achieved by inserting/extracting the

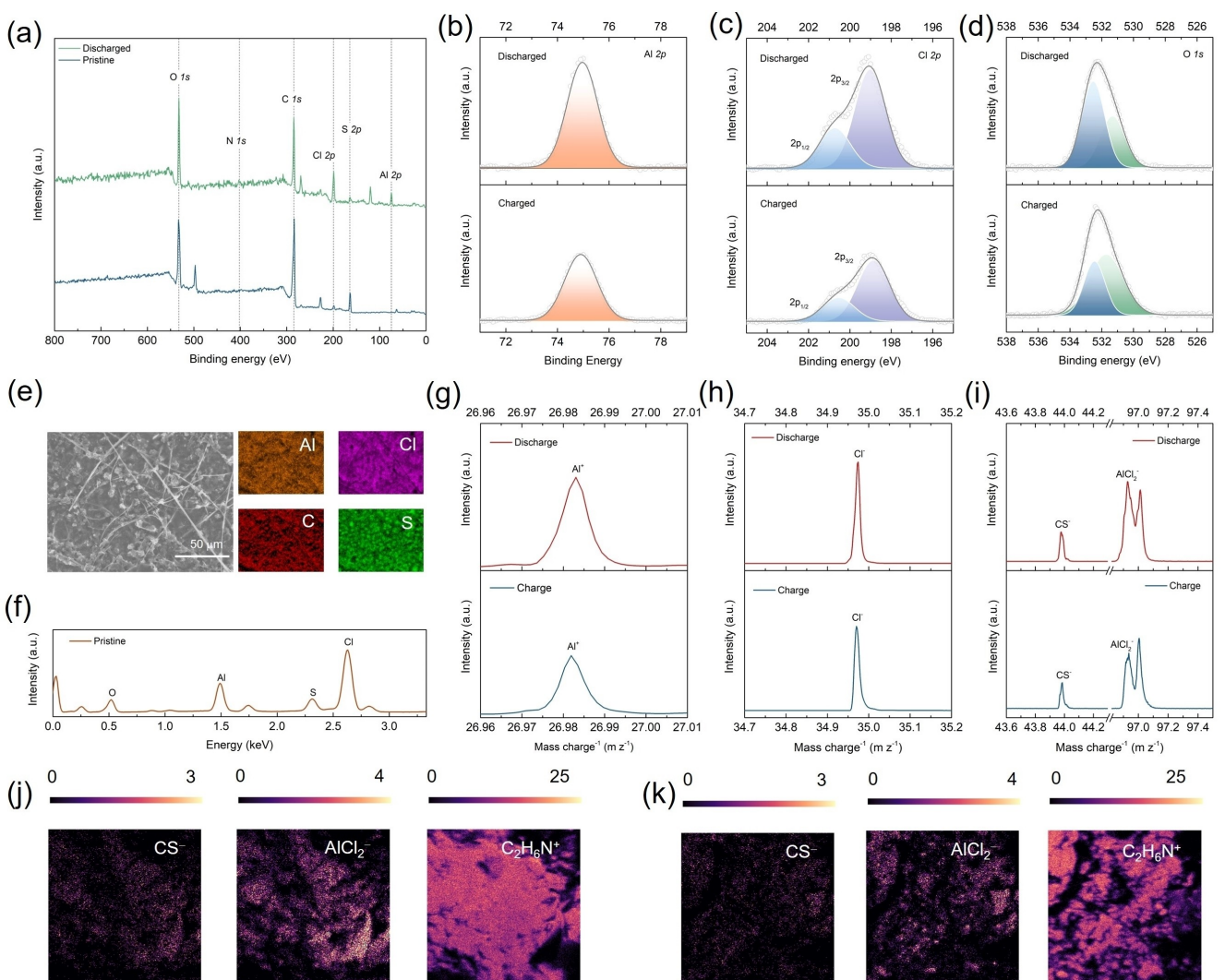


Figure 3. Characterization. a) The XPS spectrum of the discharged and the pristine BDTD electrode. b) The Al 2p spectrum, c) the Cl 2p spectrum, and d) the O 1s spectrum of the discharged and the charged electrode. e) The SEM image and the corresponding Al, Cl, C, and S elemental mappings of the discharged BDTD electrode. f) The EDX spectrum of the discharged BDTD electrode. g) The Al^+ signal from the discharged and charged electrodes on the positive ToF-SIMS mass spectrum. h) The Cl^- peaks, and i) the CS^- peaks and the AlCl_2^- peaks from the discharged and charged electrodes on the negative ToF-SIMS mass spectrum. j) The CS^- , AlCl_2^- , and $\text{C}_2\text{H}_6\text{N}^+$ ToF-SIMS mappings of the discharged electrode. k) The CS^- , AlCl_2^- , and $\text{C}_2\text{H}_6\text{N}^+$ ToF-SIMS mappings of the charged electrode.

cationic species at the oxygen active sites.^[38,39] In Figure 3(d), the O 1s peak at around 532 eV corresponds to the formation of C–O–Al,^[38] while the peak at lower binding energy is assigned to C=O.^[40] The relative intensity of C–O–Al/C=O is stronger in the discharged electrode than that in the charged electrode, demonstrating the reversible conversion at the oxygen sites during cycling. The emergence of the peak at around 493.5 cm⁻¹ in the FT-IR spectrum of the discharged BDTD electrode (Supporting Information Figure S9) further corroborates the formation of C–O–Al bond during discharge, confirming the interaction between BDTD and Al species.^[41] The C 1s spectrum of the discharged and the charged electrodes are also attached to supplement the reversible conversion between C=O and C–O–Al (SI Figure S10). The three dominant peaks correspond to various functional group: C–C/C=C at 284.8 eV, C–O/C–S at 286.4 eV and C=O/O–C=O at 289.3 eV.^[29] The ratio of the area under the C–O/C–S peak to the area under the C=O/O–C=O in the discharged electrode (approximately 10:1) is much higher than that in the charged electrode (approximately 5:1), suggesting that the C=O bonds transform into the enol bonds (C–O) upon discharge, and the C=O bonds would recover after charging. The C 1s spectra of the pristine electrode is also presented (Supporting Information Figure S11), in which the ratio of the area under the C–O/C–S peak to the area under the C=O/O–C=O is about 3:1, indicating the high reversibility of the transformation between C=O and C–O during the discharging and charging processes.

The surface morphology of the discharged electrode along with the corresponding elemental mappings are presented Figure 3(e). As shown, Al, Cl, C, and S are uniformly distributed on the discharged electrode. From the energy dispersive X-ray (EDX) spectrum presented in Figure 3(f), the Cl/Al atomic ratio is ~2.4, suggesting AlCl₂⁺ as the dominant reacting species. The atomic excess Cl beyond the stoichiometric AlCl₂⁺ is reasonably attributed to the presence of Cl in pristine BDTD (Supporting Information Figure S12) as well as residue electrolyte on the discharged electrode.

Time-of-flight secondary-ion mass spectroscopy (ToF-SIMS) was utilized to further investigate the reaction mechanism during cycling. The CS⁻ ion signal was used to benchmark the presence and distribution of BDTD, as BDTD represents the only source for S in the system. The CS⁻ signal of the pristine electrode is presented in Supporting Information Figure S13. In comparison, the discharged electrode demonstrates a stronger Al⁺- (Figure 3g) and Cl⁻ signal (Figure 3h), than the charged electrode. This is reasonably attributed to the insertion of the chloroaluminate complex species during discharge, which corroborates the XPS results. From the negative mass spectra presented in Figure 3i, the CS⁻ and the AlCl₂⁻ signals were seen in both the discharged- and the charged electrodes. In the discharged electrode, the relative intensity of AlCl₂⁻/CS⁻ is higher than that in the charged electrode, suggesting that the insertion of AlCl₂⁺ into the electrode during discharge and the extraction of AlCl₂⁺ during charge take place. The AlCl₂⁻ signal observed on the charged electrode can be due to the residue electrolyte and/or the irreversible insertion of the AlCl₂⁺ during the first discharge, which led to a decrease in reversible

capacity in the subsequent charging cycle (SI Figure S6). It is important to note that ToF-SIMS only provides qualitative information of the chemical species rather than quantitative information. Thus, the strong signal of AlCl₂⁺ may not necessarily represent the actual abundance/concentration of AlCl₂⁺ species on the samples. To demonstrate that the AlCl₂⁻ signal does not solely originate from the residue electrolyte, the CS⁻, AlCl₂⁻, and C₂H₆N⁺ mappings of the discharged- and charged electrode are presented in Figure 3(j and k), respectively. The C₂H₆N⁺ signal is used as an indicator of residue electrolyte on the cycled electrodes. The absence of C₂H₆N⁺ signal on the pristine electrode, shown in Supporting Information Figure S14, indicates that the C₂H₆N⁺ is attributed to the TMAHCl electrolyte rather than the hydrocarbon contamination on the sample. As shown in Figure 3(j and k), the distribution of AlCl⁻ overlaps with the distribution of CS⁻ in the discharged- and charged electrodes, revealing AlCl₂⁺ as the reacting species.

Cyclic voltammetry (CV) was conducted to further probe the contribution of the charge storage mechanism and the kinetics of the BDTD electrode. Two oxidation peaks (labelled as Ox 1 and Ox 2) and one reduction peak (labelled as Red 1) were observed from the CV plot (Supporting Information Figure S15a). In CV measurements, the total current measured at a fixed potential can be interpreted as a sum of the current associated with the slow diffusion-controlled faradaic process and the current used to charge the electric double layer (capacitive reactions) or from the fast faradaic reaction occurring at the electrode surface (pseudocapacitive reactions).^[42] At a fixed potential, the current responses *i* at different scan rates *v* obey the power law relationship (*i*=*av*^{*b*}), where *a* and *b* are adjustable parameters.^[43] A *b* value of 0.5 signifies the contribution of the slow diffusion-controlled charge storage process, where *i*=*av*^{0.5}. While a *b* value of 1 indicates that the charge is stored via a fast surface-controlled process, where *i*=*av*. The *b* values of Ox 1, Ox 2 and Red 1 can be determined from the slope (Supporting Information Figure S15b) by plotting the log *i* vs. log *v* graph, which are close to 0.5, suggesting that the current primarily stemmed from the diffusion-controlled faradaic reactions.

A general equation is used to account for all possible scenarios: *i*=*k₁v+k₂v*^{0.5}, from which the capacitive current response (*k₁v*) can be distinguished from the diffusion-controlled intercalation process current response (*k₂v*^{0.5}). The equation can be rearranged to be: *iv*^{-0.5}=*k₁v*^{0.5}+*k₂*. By plotting *iv*^{-0.5} versus *v*^{0.5} at each given potential, the slope obtained would be *k₁*, and *k₂* is equal to the y-axis intercept. Using this approach, the capacitive current and the diffusion-controlled current were solved at each potential for each scan rate. As shown in Figure 4(a), at 0.2 mVs⁻¹, the diffusion-controlled charge storage dominates and accounts for 80% of the total charge stored (blue-shaded portion). The diffusion-controlled charge storage contribution increases with the decreasing scan rates, contributing to 65, 72, 80 and 85% of the total charge at 1, 0.5, 0.2 and 0.1 mVs⁻¹, respectively (Figure 4b).

Quantitatively understanding the transport kinetics of the electroactive species inside the solid electrode is of great

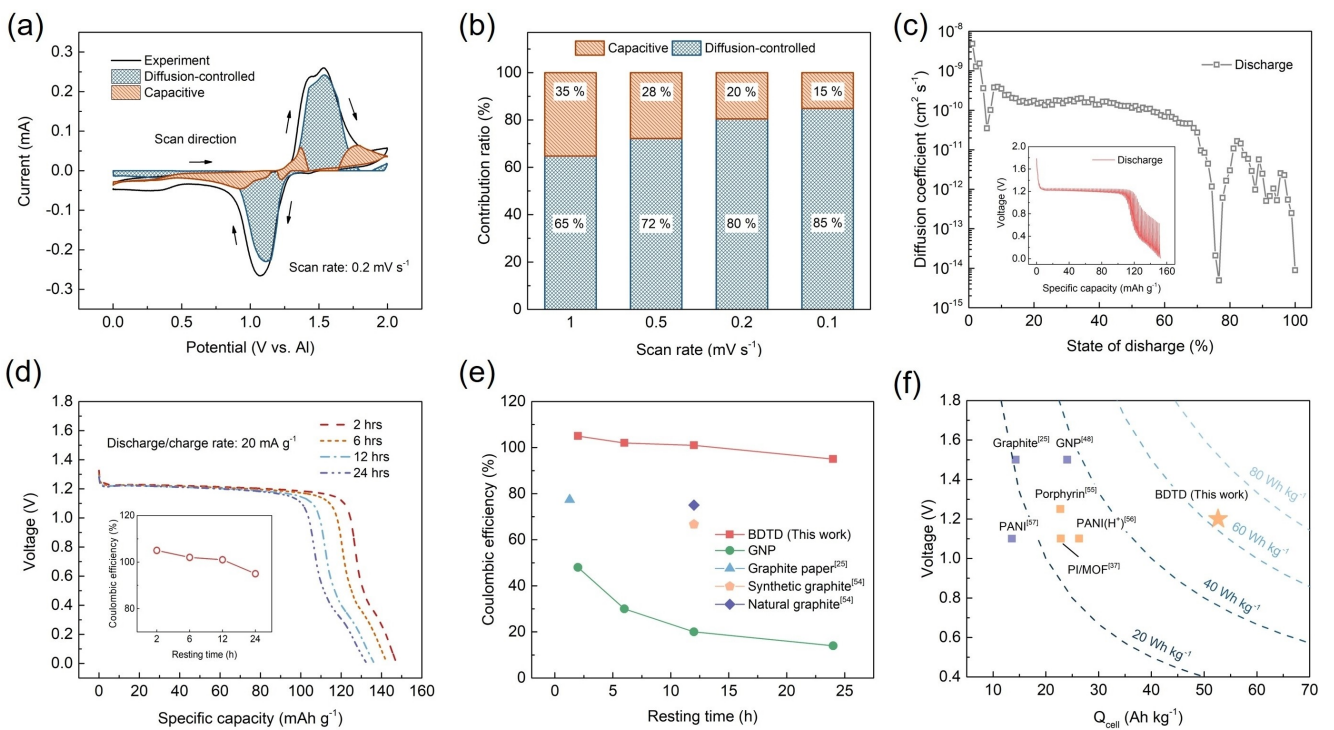


Figure 4. a) Deconvoluted diffusion-controlled and capacitive charge storage contribution in BDTD at 0.2 mV s⁻¹. b) Capacitive and diffusion-controlled contribution across scan rates of 1–0.1 mV s⁻¹. c) The GITT measurement and the corresponding voltage vs. time profile. d) Capacity retention and the corresponding Coulombic efficiencies (inset) of the fully charged BDTD electrode after resting for 2, 6, 12, and 24 h. e) Self-discharge behavior.^[25,56] f) Average discharge capacity vs. diffusive cell-level capacity of the previously reported cathode materials.^[25,38,50,57–59] Purple squares: AlCl₄⁻ intercalation type electrodes. Orange squares and star: AlCl₂⁺ intercalation type electrodes.

importance for providing fundamental insights on the transport mechanism, as well as searching and optimizing the energy storage materials. In this study, galvanostatic intermittent titration techniques (GITT) was carried out to determine the diffusion coefficient of electroactive species inside the BDTD. During the GITT measurement, the Al/BDTD battery was discharged for 5 min under a current density of 20 mA g⁻¹, followed by a 30-min relaxation. The steps were repeated until the cut-off voltage was reached.

The diffusion coefficient is determined using the Equation (1):

$$D = \frac{4}{\pi} \left(\frac{m_B V_m}{M_B S} \right)^2 \left(\frac{\Delta E_s}{\tau \left(\frac{dE}{d\sqrt{t}} \right)} \right)^2 \quad (1)$$

where D is the chemical diffusion coefficient of the electroactive species inside the active material (cm² s⁻¹); m_B is the mass of the active material (g); V_m is the molar volume of the active material (cm³ mol⁻¹); M_B is the molar mass of the active material (g mol⁻¹); S is the electrode/electrolyte contact area (cm²); ΔE_s is the change in equilibrium voltage after each titration step; τ is the duration of the current pulse (s); and $\frac{dE}{d\sqrt{t}}$ is the change in voltage versus the square root of time during the current pulse.^[44,45] When the change in cell voltage versus the square root of time exhibits linear relationship, Equation (1) can be further transformed to:

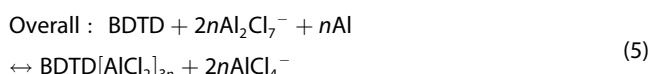
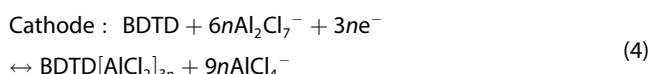
$$D = \frac{4}{\pi \tau} \left(\frac{m_B V_m}{M_B S} \right)^2 \left(\frac{\Delta E_s}{\Delta E_t} \right)^2 \quad (2)$$

where ΔE_t is the change of the cell voltage during the current pulse, neglecting the internal resistance drop. To confirm the applicability of Equation (2), the change in voltage vs. the square root of time during the titration was plotted and a linear relationship was observed (Supporting Information Figure S16). The diffusion coefficients versus the different state of discharge are plotted in Figure 4c. During discharge, the diffusion coefficients range from 4.85×10^{-9} to 4.92×10^{-15} cm² s⁻¹. The drastic drop of the diffusion coefficient at around 80% state of discharge can be explained by the vacancy diffusion mechanism, where the number of free sites for the active ion diffusion decrease with the increase of the intercalation degree.^[46] The diffusion coefficients are several orders of magnitude higher compared with the sulfide materials reported for Al³⁺ intercalation.^[47,48] Before 80% state of discharge, the diffusion kinetics is comparable to that of AlCl₄⁻ reported in natural graphite.^[49]

Unlike many other cathode materials explored in AlBs, the BDTD electrode exhibits one distinct, flat discharge voltage plateau, which correlates well with the large portion of the diffusion-controlled charge storage observed from the CV, making BDTD a battery-type material.^[42] To evaluate the charge retention capability of BDTD, a self-discharge test was performed. The cell was cycled for 5 cycles at 20 mA g⁻¹ prior

to the self-discharge test. After the previous charging cycle, the cell was rested for 2, 6, 12 and 24 h, respectively. The discharging capacities after each resting were recorded and the corresponding coulombic efficiencies are shown in the subplot (Figure 4d). After resting for 2, 6, 12 and 24 h, the BDTD electrode could still reach capacities of 147, 143, 136 and 132 mAh g⁻¹, with corresponding coulombic efficiencies kept above 95%. To highlight this extraordinary charge storage capability of the BDTD electrode, we presented the capacity retention of graphene nanoplatelet (GNP) electrode as a comparison. The highly capacitive carbonaceous cathode materials endow Al-carbonaceous cathode battery remarkable high-power density, which were being explored in a significant body of research in the past decade.^[10,50–55] The GNP electrode could only retain discharging capacities of 43, 27, 20 and 15 mAh g⁻¹, after resting for 2, 6, 12 and 24 h (Supporting Information Figure S17). The coulombic efficiencies of the corresponding cycles were 48, 30, 20 and 14%, which are much lower than those of the BDTD electrode, showing that the BDTD can retain the charge for longer time. We also summarize the previously reported self-discharge behavior of the explored material in Figure 4(e). The carbonaceous materials suffer from an inferior charge retention over resting in general: the coulombic efficiency of the graphite paper dropped to 77.35% after 4000 s resting,^[25] the capacity of the natural graphite reduced by 25% over 12-h resting; while the synthetic graphite only retained 66.7% of the capacity upon 12-h resting.^[56] The data used to plot the graph are tabulated in Supporting Information Table S2.

According to the above discussion, the electrochemical redox reactions during the discharging and the charging processes at the anode and the cathode are proposed as the following:



The corresponding theoretical anode capacity (Q_A) can be determined using Equation (6):

$$Q_A = \frac{3F}{2\left(\frac{rM_{\text{AlCl}_3} + M_{\text{TMAHCl}}}{r-1}\right) + M_{\text{Al}}} = 92.8 \text{ (in Ah kg}^{-1}) \quad (6)$$

where F is the Faraday constant ($26.8 \times 10^3 \text{ mAh mol}^{-1}$), r is the mixing ratio of AlCl_3 to TMAHCl, and M_i is the molar mass of the compound.

The diffusive cathode capacity (Q_{Diff}) is estimated using the maximum cathode capacity (Q_C) and the highest diffusive charge storage contribution [Eq. (7)]:

$$Q_{\text{Diff}} = 143 \times 0.85 = 121.6 \text{ Ah kg}^{-1} \quad (7)$$

The diffusive cell-level theoretical capacity at active materials level can be determined using Eq. (8):

$$Q_{\text{cell}} = \frac{Q_A Q_{\text{Diff}}}{Q_A + Q_{\text{Diff}}} = 52.6 \text{ Ah kg}^{-1} \quad (8)$$

The cell-level energy density at active materials level can be calculated using Equation (9):

$$E_{\text{cell}} = V_{\text{avg}} \times Q_{\text{cell}} = 1.2 \times 52.6 = 63.1 \text{ Wh kg}^{-1} \quad (9)$$

Given the reported materials were evaluated in varied configurations (coin cell or soft package), the comparison of the cell-level energy density was conducted at active materials level. In the context of this manuscript, we would like to highlight the high energy rating of the BDTD electrode among the reported materials, which makes BDTD a promising electrode for practical applications. Such excellent charge retention is attributed to the high diffusion-controlled charge storage of the BDTD electrode. Therefore, we calculated and compared the diffusion-controlled cell-level energy density of the reported electrodes and emphasize the high energy rating of the BDTD electrode.

To highlight the superior capacity retention of BDTD, we compared the cell-level diffusive capacity and the corresponding achievable energy density at cell-level across varied kinds of electrodes (Figure 4f). The BDTD possesses high diffusive energy density among the AlCl_2^+ intercalation type electrodes.^[38,57,58] Detailed data for constructing the graph are tabulated in Supporting Information Table S3. The intercalation of AlCl_4^- fundamentally limits the attainable anode side capacity; thus, compromising the achievable cell-level theoretical capacity and energy density.^[25,50,59] The partial utilization of the capacity of Al metal and the high diffusive charge storage contribution endow BDTD a high cell-level energy density.

Conclusion

In this study, we investigated the electrochemical performance and the charge storage mechanism of BDTD as a cathode material in ALBs. The BDTD exhibits an initial capacity of 143 mAh g⁻¹ and possesses a flat discharge voltage plateau at around 1.2 V (vs. Al/Al³⁺). The Super PTM-modified membrane is proven to be an effective strategy to enhance the overall electrochemical performance of the cell. The BDTD retains >95% of the previous charging cycle after resting for 24 h, demonstrating a good capacity retention. Ex-situ XPS, FT-IR, SEM-EDX, and ToF-SIMS were conducted to understand the underlying charge storage mechanism of the BDTD in $\text{AlCl}_3/\text{TMAHCl}=1.8$ chloroaluminate IL electrolyte. The AlCl_2^+ is identified as the charge carrier ion, which reversibly interact with the carbonyl (C=O) group and contributes to the reversible capacity. To further improve the electrochemical performance of the BDTD electrode, several recommendations are made to address the capacity loss due to the shuttling of the dissolved active material. Fabricating composite electrode

could potentially enhance the stability of organic active material as the skeleton of metal-organic frameworks was reported to effectively slow down the dissolution of polyimide in ionic liquid electrolyte.^[38] Successful implementation of selective permeable thin film made of polymeric materials on the membrane that encapsulates the active material would potentially enhance the cyclability of the organic electrode.^[60] This work demonstrates a novel Al-organic battery with high diffusive cell-level energy density, which paves the road for developing alternative organic materials with low self-discharge rate for practical application.

Acknowledgements

The authors acknowledge the financial support from Ministry of Economic Development, Job Creation and Trade (Grant No. 504535) and XSeed grant provided by the University of Toronto. The authors thank Dr. Raiden Acosta for his assistance with XRD, Dr. Peter Brodersen for his assistance on XPS and ToF-SIMS characterization, and Dr. Mengsha Li for SEM characterization.

Conflict of Interest

The authors declare no conflict of interest.

Data Availability Statement

The data that support the findings of this study are available from the corresponding author upon reasonable request.

Keywords: aluminum • aluminum-ion batteries • energy storage • intercalations • organic electrode

- [1] J. Xie, Y.-C. Lu, *Nat. Commun.* **2020**, *11*, 1–4.
- [2] “Outlook for electricity – world energy outlook 2020 – analysis – IEA,” can be found under <https://www.iea.org/reports/world-energy-outlook-2020/outlook-for-electricity#abstract>, n.d.
- [3] F. Duffner, N. Kronemeyer, J. Tübke, J. Leker, M. Winter, R. Schmuck, *Nat. Energy* **2021**, *6*, 123–134.
- [4] C. Helbig, A. M. Bradshaw, L. Wetschel, A. Thorenz, A. Tuma, *J. Cleaner Prod.* **2018**, *172*, 274–286.
- [5] B. E. Murdock, K. E. Toghill, N. Tapia-Ruiz, *Adv. Energy Mater.* **2021**, *11*, 2102028.
- [6] Y. Liang, H. Dong, D. Aurbach, Y. Yao, *Nat. Energy* **2020**, *5*, 646–656.
- [7] S. K. Das, S. Mahapatra, H. Lahan, *J. Mater. Chem. A* **2017**, *5*, 6347–6367.
- [8] Y. Zhang, S. Liu, Y. Ji, J. Ma, H. Yu, *Adv. Mater.* **2018**, *30*, 1706310.
- [9] K. L. Ng, B. Amirthraj, G. Azimi, *Joule* **2022**, *6*, DOI 10.1016/J.JOULE.2021.12.003.
- [10] M.-C. Lin, M. Gong, B. Lu, Y. Wu, D.-Y. Wang, M. Guan, M. Angell, C. Chen, J. Yang, B.-J. Hwang, H. Dai, *Nature* **2015**, *520*, 325–8.
- [11] K. V. Kravchyk, C. Seno, M. V. Kovalenko, *ACS Energy Lett.* **2020**, *5*, 545–549.
- [12] K. V. Kravchyk, M. V. Kovalenko, *Commun. Chem.* **2020**, *3*, 1–9.
- [13] Z. Rong, R. Malik, P. Canepa, G. Sai Gautam, M. Liu, A. Jain, K. Persson, G. Ceder, *Chem. Mater.* **2015**, *27*, 6016–6021.
- [14] G. A. Elia, K. V. Kravchyk, M. V. Kovalenko, J. Chacón, A. Holland, R. G. A. Wills, *J. Power Sources* **2021**, *481*, 228870.
- [15] L. Geng, J. P. Scheifers, C. Fu, J. Zhang, B. P. T. Fokwa, J. Guo, *ACS Appl. Mater. Interfaces* **2017**, *9*, 21251–21257.
- [16] H. Yang, L. Yin, J. Liang, Z. Sun, Y. Wang, H. Li, K. He, L. Ma, Z. Peng, S. Qiu, C. Sun, H.-M. Cheng, F. Li, *Angew. Chem. Int. Ed.* **2018**, *57*, 1916–1920; *Angew. Chem. Int. Ed.* **2018**, *57*, 1898–1902.
- [17] N. Zhu, F. Wu, Z. Wang, L. Ling, H. Yang, Y. Gao, S. Guo, Iumin Suo, H. Li, H. Xu, Y. Bai, C. Wu, *J. Energy Chem.* **2020**, *51*, 72–80.
- [18] A. Colmenar-Santos, A. M. Muñoz-Gómez, E. Rosales-Asensio, Á. López-Rey, *Energy* **2019**, *183*, 61–74.
- [19] X. Huo, X. Wang, Z. Li, J. Liu, J. Li, *Nanoscale* **2020**, *12*, 3387–3399.
- [20] X. Zhang, S. Jiao, J. Tu, W.-L. Song, X. Xiao, S. Li, M. Wang, H. Lei, D. Tian, H. Chen, D. Fang, *Energy Environ. Sci.* **2019**, *12*, 1918–1927.
- [21] S. Wang, S. Jiao, J. Wang, H. Sen Chen, D. Tian, H. Lei, D. N. Fang, *ACS Nano* **2017**, *11*, 469–477.
- [22] H. Lei, M. Wang, J. Tu, S. Jiao, *Sustain. Energy Fuels* **2019**, *3*, 2717–2724.
- [23] S. Jiao, H. Lei, J. Tu, J. Zhu, J. Wang, X. Mao, *Carbon* **2016**, *109*, 276–281.
- [24] S. Wang, S. Jiao, W. L. Song, H. Sen Chen, J. Tu, D. Tian, H. Jiao, C. Fu, D. N. Fang, *Energy Storage Mater.* **2018**, *12*, 119–127.
- [25] Z. Li, J. Liu, B. Niu, J. Li, F. Kang, *Small* **2018**, *14*, 1800745.
- [26] K. Qin, J. Huang, K. Holguin, C. Luo, *Energy Environ. Sci.* **2020**, *13*, 3950–3992.
- [27] Y.-T. Kao, S. B. Patil, C.-Y. An, S.-K. Huang, J.-C. Lin, T.-S. Lee, Y.-C. Lee, H.-L. Chou, C.-W. Chen, Y. J. Chang, Y.-H. Lai, D.-Y. Wang, *ACS Appl. Mater. Interfaces* **2020**, *12*, 25853–25860.
- [28] K. L. Ng, Z. Lu, Y. Wang, C. V. Singh, G. Azimi, *J. Phys. Chem. C* **2021**, *125*, 15145–15154.
- [29] S. Li, X. Wang, L. Hou, X. Zhang, Y. Zhou, Y. Yang, Z. Hu, *Electrochim. Acta* **2019**, *317*, 437–448.
- [30] X. Chen, Y. Wu, Z. Huang, X. Yang, W. Li, L. C. Yu, R. Zeng, Y. Luo, S. L. Chou, *J. Mater. Chem. A* **2016**, *4*, 18409–18415.
- [31] A. L. Ramirez, B. C. Chan, D. T. De Lill, *Acta Crystallogr. Sect. E* **2012**, *68*, o1428–o1428.
- [32] S.-B. Yoon, J.-P. Jegal, K. C. Roh, K.-B. Kim, *J. Electrochem. Soc.* **2014**, *161*, H207.
- [33] J. Smajic, S. Wee, F. R. F. Simoes, M. N. Hedhili, N. Wehbe, E. Abou-Hamad, P. M. F. J. Costa, *ACS Appl. Energ. Mater.* **2020**, *3*, 6805–6814.
- [34] Y. Hu, B. Luo, D. Ye, X. Zhu, M. Lyu, L. Wang, *Adv. Mater.* **2017**, *29*, 1606132.
- [35] L. Xing, K. A. Owusu, X. Liu, J. Meng, K. Wang, Q. An, L. Mai, *Nano Energy* **2021**, *79*, 105384.
- [36] Y. Wang, C. Fang, Y. Huang, Q. Liu, R. Zhao, X. Ding, Y. Huang, *RSC Adv.* **2018**, *8*, 24900–24905.
- [37] D.-J. Yoo, M. Heeney, F. Glöcklhofer, J. W. Choi, *Nat. Commun.* **2021**, *12*, 1–9.
- [38] J. Zhou, X. Yu, J. Zhou, B. Lu, *Energy Storage Mater.* **2020**, *31*, 58–63.
- [39] L. Zhou, Z. Zhang, L. Cui, F. Xiong, Q. An, Z. Zhou, X.-F. Yu, P. K. Chu, K. Zhang, *Cell Reports Phys. Sci.* **2021**, *2*, 100354.
- [40] J. Bitenc, N. Lindahl, A. Vizintin, M. E. Abdelhamid, R. Dominko, P. Johansson, *Energy Storage Mater.* **2020**, *24*, 379–383.
- [41] I. Rutkowska, J. Marchewka, P. Jeleń, M. Odziomek, M. Korpyś, J. Paczkowska, M. Sitarz, *Materia* **2021**, *14*, 1761.
- [42] J. Liu, J. Wang, C. Xu, H. Jiang, C. Li, L. Zhang, J. Lin, Z. X. Shen, *Adv. Sci.* **2018**, *5*, 1700322.
- [43] H. Lindström, S. Södergren, A. Solbrand, H. Rensmo, J. Hjelm, A. Hagfeldt, S.-E. Lindquist, *J. Phys. Chem. B* **1997**, *101*, 7717–7722.
- [44] W. Weppner, R. A. Huggins, *J. Electrochem. Soc.* **1977**, *124*, 1569.
- [45] Y.-S. Lee, K.-S. Ryu, *Sci. Rep.* **2017**, *7*, 1–13.
- [46] A. Hess, Q. Roode-Gutzmer, C. Heubner, M. Schneider, A. Michaelis, M. Bobeth, G. Cuniberti, *J. Power Sources* **2015**, *299*, 156–161.
- [47] H. Li, H. Yang, Z. Sun, Y. Shi, H. M. Cheng, F. Li, *Nano Energy* **2019**, *56*, 100–108.
- [48] B. Lee, H. R. Lee, T. Yim, J. H. Kim, J. G. Lee, K. Y. Chung, B. W. Cho, S. H. Oh, *J. Electrochem. Soc.* **2016**, *163*, A1070–A1076.
- [49] H. Hu, T. Cai, P. Bai, J. Xu, S. Ge, H. Hu, M. Wu, Q. Xue, Z. Yan, X. Gao, W. Xing, *Chem. Commun.* **2020**, *56*, 1593–1596.
- [50] K. L. Ng, T. Dong, J. Anawati, G. Azimi, *Adv. Sustainable Syst.* **2020**, *4*, 2000074.
- [51] Z. Liu, J. Wang, H. Ding, S. Chen, X. Yu, B. Lu, *ACS Nano* **2018**, *12*, 8456–8466.
- [52] H. Chen, F. Guo, Y. Liu, T. Huang, B. Zheng, N. Ananth, Z. Xu, W. Gao, C. Gao, *Adv. Mater.* **2017**, *29*, 1605958.
- [53] N. P. Stadie, S. Wang, K. V. Kravchyk, M. V. Kovalenko, *ACS Nano* **2017**, *11*, 1911–1919.
- [54] Y. Uemura, C. Y. Chen, Y. Hashimoto, T. Tsuda, H. Matsumoto, S. Kuwabata, *ACS Appl. Energ. Mater.* **2018**, *1*, 2269–2274.

- [55] H. Xu, H. Chen, H. Lai, Z. Li, X. Dong, S. Cai, X. Chu, C. Gao, *J. Energy Chem.* **2020**, *45*, 40–44.
- [56] J. Shi, J. Zhang, J. Guo, *ACS Energy Lett.* **2019**, *4*, 2124–2129.
- [57] X. Han, S. Li, W.-L. Song, N. Chen, H. Chen, S. Huang, S. Jiao, *Adv. Energy Mater.* **2021**, *11*, 2101446.
- [58] S. Wang, S. Huang, M. Yao, Y. Zhang, Z. Niu, *Angew. Chem.* **2020**, *132*, 11898–11905; *Angew. Chem. Int. Ed.* **2020**, *59*, 11800–11807.
- [59] Y. Liao, D. Wang, X. Li, S. Tian, H. Hu, D. Kong, T. Cai, P. Dai, H. Ren, H. Hu, Y. Li, Q. Xue, Z. Yan, X. Gao, W. Xing, *J. Power Sources* **2020**, *477*, 228702.
- [60] C. Wang, C. Jiang, Y. Xu, L. Liang, M. Zhou, J. Jiang, S. Singh, H. Zhao, A. Schober, Y. Lei, *Adv. Mater.* **2016**, *28*, 9182–9187.

Manuscript received: April 19, 2022
Accepted manuscript online: April 28, 2022
Version of record online: May 26, 2022